Optical force sensor based on plasmon modulated upconversion luminescence

Conrad Corbella Bagot[1], Taleb Ba Tis[2], Bo Xu[3], Cobi Sabo[1], Eric Rappeport[1] and Wounjhang Park[1,2,4,*]
[1]Department of Electrical, Computer and Energy Engineering
[2]Materials Science and Engineering Program
[3]Department of Physics
[4]Biomedical Engineering Program
University of Colorado, Boulder, CO 80309-0425, U.S.A.
[*]won.park@colorado.edu

Abstract
We report a novel force sensor exploiting the interaction between plasmonic nanostructures and upconversion nanoparticles (UCNPs). The nanosensor is composed of a gold nanodisk and UCNPs separated by a flexible polymer layer. The gold nanodisk is designed to exhibit a plasmon resonance that selectively enhances one of the emission bands of the UCNPs while leaving the other ones largely unaffected. As the nanosensor is compressed or stretched by an external force, the polymer layer thickness changes, modulating the plasmon-UCNP coupling. The resulting changes in the luminescence intensity provides the basis for sensing. Furthermore, the nanosensor employs ratiometric sensing which makes it highly robust against any environmental variations. Our nanosensors exhibit two orders of magnitude higher responsivity than previously reported UCNP-based force sensors. They can be prepared as an on-chip sensor array or in a colloidal solution, making them suitable for a variety of applications in biology and robotics.

Keywords
Upconversion luminescence, plasmon, force sensing

Upconverting nanoparticles (UCNPs) are excited by infrared light and emit visible and ultraviolet photons. The use of infrared excitation is attractive for chemical and biological sensing as it is absorbed minimally by water and many organic compounds and does not induce any background autofluorescence, leading to superior signal-to-noise ratio.[1] Compared to other frequency upconversion mechanisms such as two-photon fluorescence and high harmonic generation, UCNPs show far greater efficiencies.[2] Furthermore, UCNPs do not photobleach or blink, making them ideal agents for imaging and sensing.[3] Considering these advantages, it is unsurprising that research on UCNP-based sensors has been steadily increasing over the years.[4]

Most UCNP-based sensors rely on the same principle – energy transfer between the rare earth ions within UCNPs and the molecules attached to their surface. Any mechanism that alters the rate of energy transfer can therefore be used for sensing. A commonly used mechanism is the modification of spectral overlap between the rare earth ions and the sensing molecules in response to a change in the environmental conditions. For example, fluorescein isothiocyanate (FITC) is known to exhibit significant changes in the absorption in the blue spectrum as the pH is varied. This has been used to demonstrate pH sensing with FITC-coated UCNPs.[5] Similarly, Hg sensing has been performed by using a Ru(II) complex that exhibits a shift in the absorption band in the presence of Hg^{2+} ions.[6] In both cases, changes in the absorption properties of the sensing molecule modifies the spectral overlap, which in turn alters the energy transfer rate. Another commonly employed mechanism exploits the strong distance dependence of the energy transfer rate. In this scheme, efficient energy transfer takes place only when the sensing molecules bind on the UCNP surface via, for example, nucleic acid interaction[7] or antibody-antigen interaction.[8] The energy transfer then alters the luminescence from UCNPs, enabling sensing operation.

An alternative approach for UCNP-based sensing is to use the optical interaction between UCNPs and photonic nanostructures that support strong resonances. The optical interaction can affect all aspects of upconversion including absorption, emission, and energy transfer between rare earth ions.[9] Any mechanism that alters the strength of the optical interaction can thus be used for sensing applications. In this paper, we present a sensing platform based on the Purcell effect, which influences the emission process. Since the optical interaction responsible for the Purcell effect is a short-range interaction with strong distance dependence, any changes in the distance between the UCNPs and the nanoresonator modifies the luminescence properties. To build a sensor based on this mechanism, one should employ a molecule or a material that changes its length or volume in response to the environmental conditions or analytes one wants to detect. In this work, we report a straightforward yet powerful example of this sensing scheme which allows optical detection of mechanical forces. Sensors capable of quantitatively measuring physical forces are critical for a wide range of fields such as biology, medicine, and robotics. In biology and medicine, the interplay between physical forces and cell functions has long been a fundamental subject of research.[10] Physical forces play an important role in many biological processes such as stem cell differentiation,[11] initiation of transcriptional programs,[12] morphogenesis,[13] cell migration,[14] malignancy[15], and wound healing.[16] In robotics, high quality tactile sensing would enable more delicate and complex operations such as grasp control, dexterous manipulation or object recognition.[17]

Thanks to the short-range nature of plasmonic interaction, our nanosensor is responsive to small changes in the geometry, enabling the detection of small forces. Recently, it was reported that Mn co-doped UCNPs and alkaline earth UCNPs can sense forces in the range of 100 nN to 10 μN.[18] In this work, we report sensing forces in the similar range but with much higher force responsivities of 0.3~2 μN^{-1}, representing up to two orders of magnitude improvement. Additionally, nanoscale sensors naturally provide high spatial resolution. We also developed an ingenuous fabrication technique that combines lithography, nanoparticle self-assembly, and nanopattern transfer to produce a massive array of 100 million to 1 billion nanosensors. The as-fabricated nanosensor array will be suitable for cell culture experiments for biology and many robotics applications. Furthermore, the nanosensors can eventually be dispersed in water for direct injection into tissues for *in vivo* experiments.

Sensing principle and sensor design

Light emission near a metal nanostructure is affected by the interplay between the positive effect of plasmon enhancement and the negative effect of quenching.[9b, 19] Specifically, in the vicinity of a plasmonic nanostructure, radiative transition rates can be enhanced by the increased density of photonic states – a phenomenon known as the Purcell effect.[20] On the other hand, the metal also provides an additional nonradiative decay path, leading to luminescence quenching. In general, quenching tends to dominate at very short distances while the Purcell enhancement prevails at slightly larger distances.[21]

With this principle in mind, we performed numerical simulations to design the sensor such that the plasmon resonance selectively enhances one of the luminescence bands while leaving the other emission band largely unaffected. The sensor's signal is given by the intensity ratio of the two bands. By using the unaffected luminescence as a reference, the signal is automatically calibrated against any variations in the luminescent probe density or environmental effects such as the presence of a strongly absorbing material. This ratiometric sensing approach thus allows much more robust and precise sensing than the simple fluorescence intensity-based sensing. The effectiveness of ratiometric sensing with UCNPs has recently been demonstrated.[22]

Our nanosensor is composed of a gold nanodisk, a polydimethylsiloxane (PDMS) layer and UCNPs (Figure 1a). The UNCPs are $NaYF_4:Yb^{3+},Tm^{3+}$ nanoparticles which, under 980 nm excitation, emit multiple luminescence bands, as shown in Figure 1(b). In this work, we use the two strongest emission bands centered at 645 and 800 nm. These emissions exhibit better tissue penetration, and allow the use of larger gold nanodisk, making the fabrication process less challenging. The finite-difference time-domain (FDTD) simulations showed that a gold nanodisk with a diameter of 150 nm and a thickness of 30 nm is the best choice. As shown in Figure 1(c), the nanosensor structure exhibits a main plasmonic peak centered at around 770 nm and a smaller peak near 610 nm. The PL intensity ratio decays exponentially with distance from the metal surface, following the local field profile, as shown in Figure 1(d). The nanosensor is responsive

over PDMS thicknesses between 10 and 60 nm, while being more sensitive at small thicknesses. This distance dependent PL intensity ratio provides the basis for the force sensing.

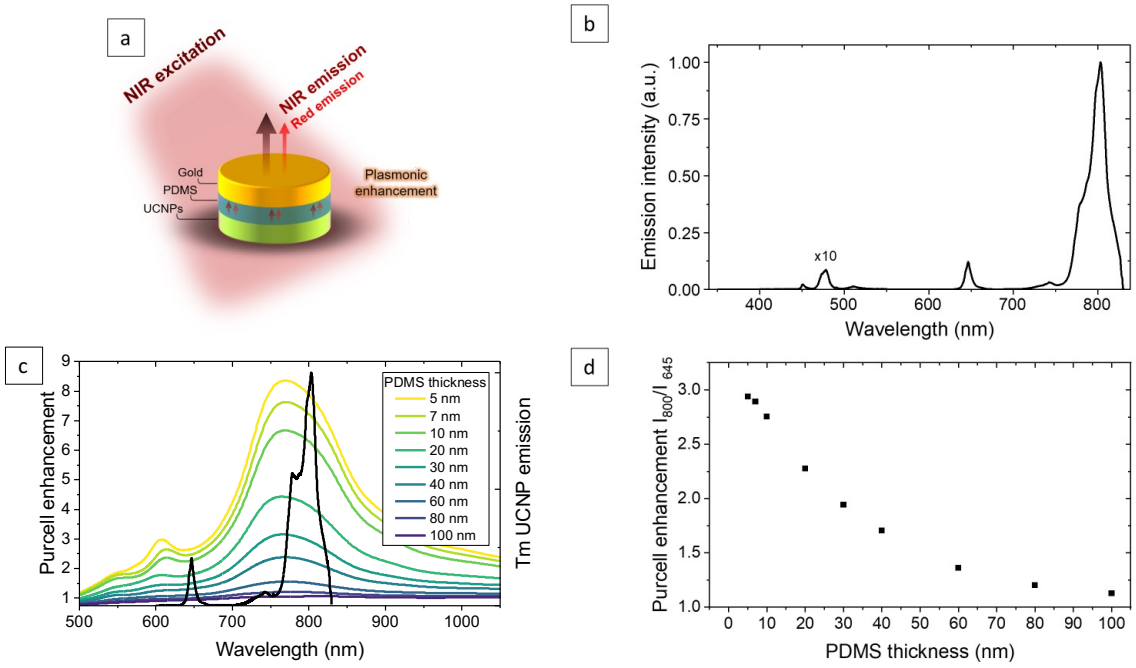

Figure 1. Design of the force sensor. (a) Schematic of the nanosensor composed of a gold nanodisk, a flexible polymer (PDMS), and UCNPs. The gold nanodisk supports a plasmon resonance that selectively enhances the near-infrared (800 nm) emission of UCNP while minimally affecting the visible (645 nm) emission. Since the plasmon enhancement is highly sensitive to the separation between UCNP and gold nanodisk, the photoluminescence (PL) intensity ratio, I_{800}/I_{645}, can be used to determine the thickness of the PDMS layer from which the applied force can be extracted. (b) PL spectrum of $NaYF_4:Yb^{3+},Tm^{3+}$ UNCP under 980 nm excitation. Among the multiple emission bands, 645 and 800 nm are used for sensing. The blue portion of the spectrum was magnified to facilitate its visualization (x10). (c) Calculated Purcell enhancement factor for various PDMS thicknesses. The size of the gold nanodisk is chosen to exhibit a large enhancement at 800 nm and minimal enhancement at 645 nm. That is, the gold disks are 150 nm in diameter and 30 nm in thickness. (d) Simulated PL intensity ratio, I_{800}/I_{645}, as a function of PDMS thickness. It shows the typical exponential dependence on the thickness and thus the sensor is most effective between 10 and 60 nm thickness of PDMS.

Sensor fabrication

To make the nanosensors, we developed a novel fabrication process that combines laser interference lithography (LIL), self-assembly of UCNPs, pattern transfer and dry/wet etching. The process flow is schematically shown in Figure 2. First, a nanohole array pattern on photoresist (PR) was fabricated by LIL. Then, gold deposition and lift-off were used to produce an array of gold nanodisks on a silicon substrate. We have previously used this process for the fabrication of metal-insulator-metal (MIM) structures.[23] In parallel, we synthesized $NaYF_4:Yb^{3+},Tm^{3+}$ UCNPs using the co-precipitation method.[5b, 24] The UCNPs have a tight size distribution, 32.6 ± 1.6 nm

(Figure S1). The UCNPs were self-assembled into a monolayer using the interfacial self-assembly method.[25] We then spin-coated a thin layer of PDMS on top of the UCNP monolayer. Next, we transferred the gold nanodisks onto the PDMS surface using polymethyl methacrylate (PMMA) as the transfer medium. For this, we modified a process originally developed for MoS_2 transfer.[26] Before the transfer, the PDMS surface is lightly treated with O_2 plasma to ensure good adhesion between PDMS and the gold nanodisks. After the gold nanodisk transfer process, we need to remove the extra PDMS and UCNPs outside the gold nanodisks. This was achieved by reactive ion etching using CF_4 which removes PDMS and then wet etching with HCl that removes UCNPs. During these etching steps, the gold nanodisks act as etch masks, protecting the PDMS and UCNPs underneath them. At this point, we have an array of nanosensors on a glass substrate, which can be used for biosensing with live cell cultures or non-biological applications in robotics. For *in vivo* biosensing applications which requires colloidal sensors, we can use polyvinyl alcohol (PVA) to lift the sensors off the substrate and disperse them in water, as we have demonstrated with the MIM structures previously.[23] It is also possible to conjugate the nanosensors with functional biomolecules, as we have previously shown in the targeted optoporation of bladder cancer.[27] A detailed description of the fabrication process is given in the Supporting Information.

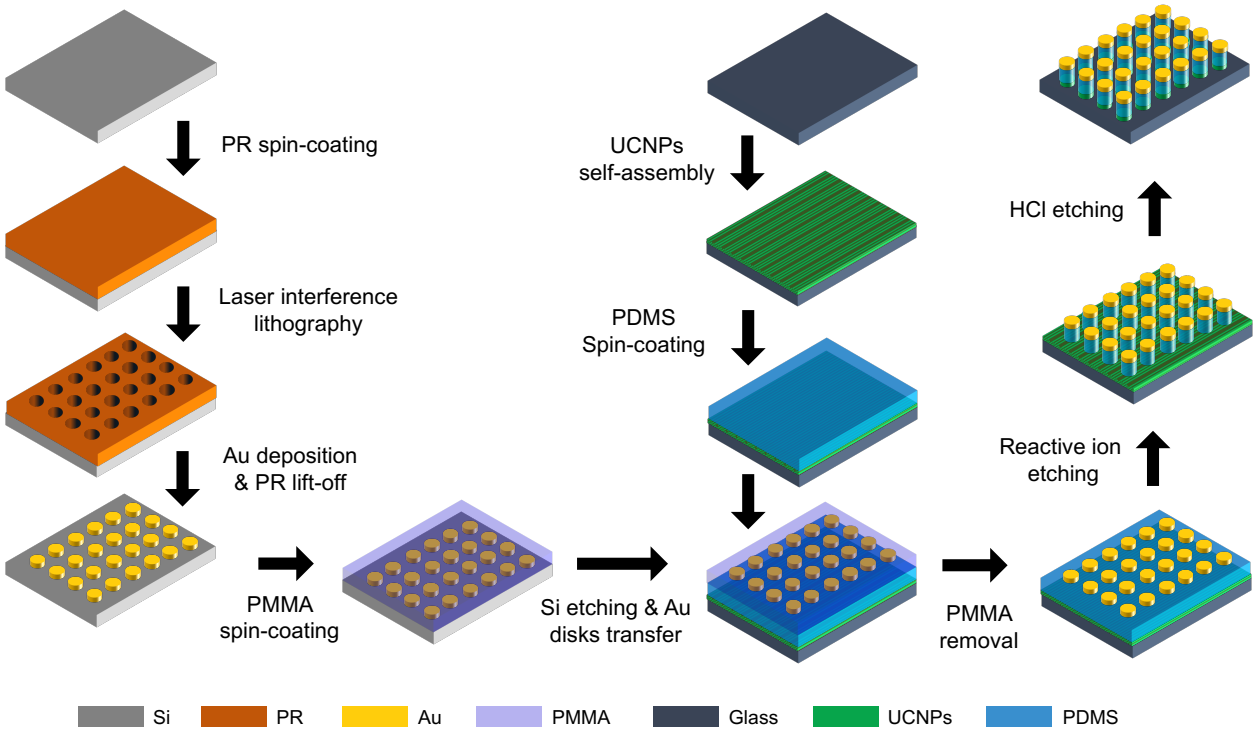

Figure 2. Schematic of the fabrication process. First, laser interference lithography is used to produce a nanohole array on a silicon substrate. A subsequent gold evaporation and lift-off yields an array of gold nanodisks on silicon. In parallel, UCNP monolayer is self-assembled using the interfacial self-assembly method and a thin layer of PDMS is spin-coated on top of the UCNP monolayer. The gold nanodisks are then transferred onto the PDMS surface using PMMA as the transfer medium. Finally, the PDMS and UCNPs located outside the gold nanodisks are removed by reactive ion etching with CF_4 and wet etching by HCl.

Figure 3 shows the samples at various stages of the fabrication process. Figure 3(a) shows the nanohole array fabricated by LIL. The average hole diameter was 152 ± 4 nm (Figure S2). As shown in the inset, the sidewalls are either vertical or slightly tiled inward. Furthermore, the sidewall profile shows modulation due to the interference between the incident and reflected light. Both of these features help prevent the formation of continuous gold film in the subsequent gold evaporation, making the lift-off process reliable and repeatable. Figure 3(b) shows the gold nanodisks after lift-off. The diameter was 153 ± 4 nm (Figure S2). The self-assembled monolayer of UCNPs is shown in Figure 3(c). We were able to achieve densely packed monolayer of UCNPs but the UCNPs did not form a highly ordered array. It is generally difficult to obtain a highly ordered array of small nanoparticles because they tend to lack well-defined edges. The quality of our monolayer appears to be similar to that reported by Ye et al.[28] and much better than what was first achieved by this technique.[25] Importantly, the presence of some disorder is not critical in our work because we adopted ratiometric sensing. A large variation in the nanoparticle density will result in an equally large variation in luminescence intensity, which is detrimental to intensity-based sensing. However, in ratiometric sensing, any variations in nanoparticle density and other environmental effects cancel out, yielding a highly robust signal. We have previously shown that the PL intensity variations in our self-assembled monolayer was around 18% but the PL intensity ratio varied by 3%.[22] Thus, the presence of disorder in the monolayer is not critical in our nanosensors. Figure 3(d) shows the PDMS film on UCNPs. By controlling the PDMS concentration and spin speed, we were able to obtain uniform thin films with thicknesses between 15 and 60 nm. Figure 3(e) shows the transferred gold nanodisks after the PDMS etching and Figure 3(f) is the final nanosensor array after etching both PDMS and UCNPs outside the gold nanodisks. The fabricated nanosensors were finally characterized by atomic force microscopy (AFM). The AFM topology scan not only confirmed that the background PDMS and UCNPs were fully etched but also gave the total height of the nanosensor. As shown in Figure S3, the sensor height exhibits ±5 nm or 6% variations.

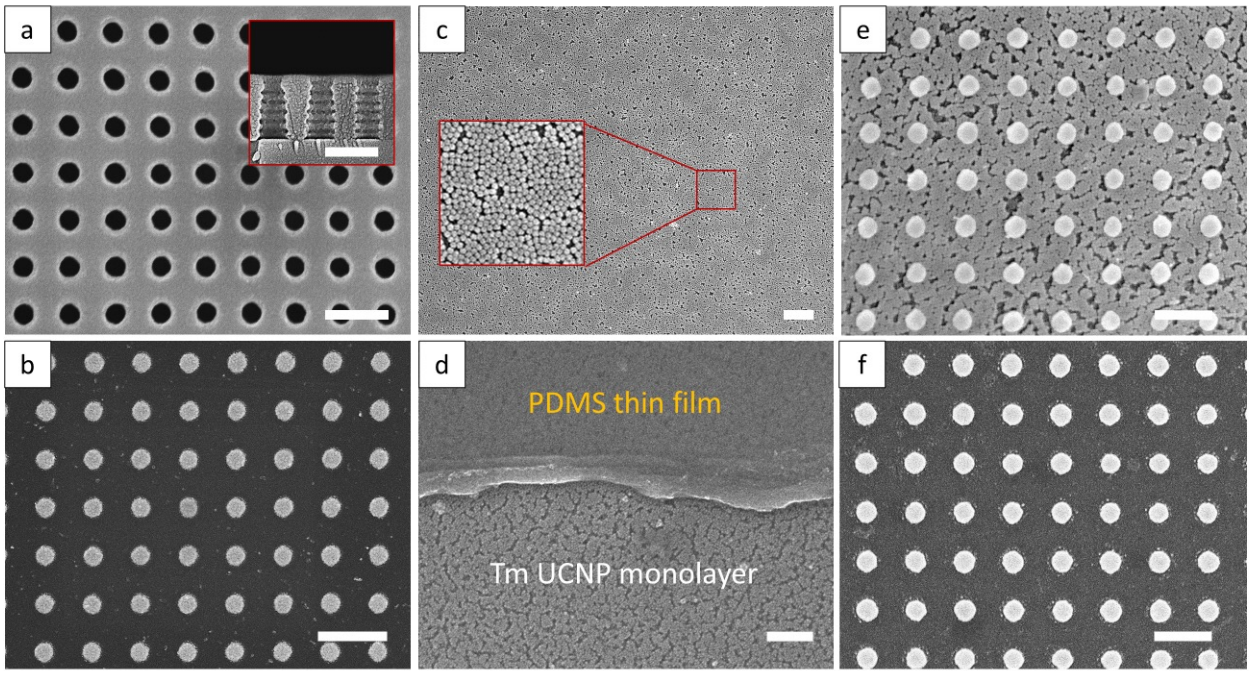

Figure 3. Scanning electron micrographs (SEMs) of (a) nanohole array on a negative photoresist produced by laser interference lithography (Inset: cross-sectional view of the nanoholes revealing the modulated sidewall profile due to the interference pattern), (b) gold nanodisk array obtained by gold evaporation on the nanohole array shown in (a) and a subsequent lift-off, (c) monolayer of UCNPs obtained by the interfacial self-assembly method (Inset: a higher magnification view of the self-assembled monolayer), (d) PDMS thin film deposited on the UCNP monolayer shown in (c). Here, we deliberately etched the PDMS layer partially to reveal the underlying UCNP monolayer for better visualization. (e) Gold nanodisks transferred onto the PDMS surface after dry etch and (f) the final sensor array after etching away the extra UCNPs outside the gold nanodisks. All scale bars indicate 500 nm.

Sensor characterizations

The fabricated nanosensors were characterized by using a confocal microscope coupled to a spectrometer. Figure 4(a) and (b) show the optical micrographs of the fabricated nanosensor array. The entire array is roughly 4 mm x 7 mm, containing ~280 million nanosensors. Figure 4(c) shows the PL spectra of a UCNP monolayer and the nanosensor under 980 nm excitation, normalized to the 645 nm emission peak. It clearly shows that the plasmon resonance enhances the 800 nm peak relative to the 645 nm. This selective enhancement is the key to the operation of our nanosensor. Figure 4(b) shows that the nanosensor array exhibits remarkable uniformity with PL ratio variations of around 5%. This is due in part to the structural uniformity as described earlier in the fabrication section and also to the self-calibration effect of ratiometric sensing. Most of these variations are believed to arise from the nonuniformity of PDMS thickness, which leads to changes in PL enhancement.

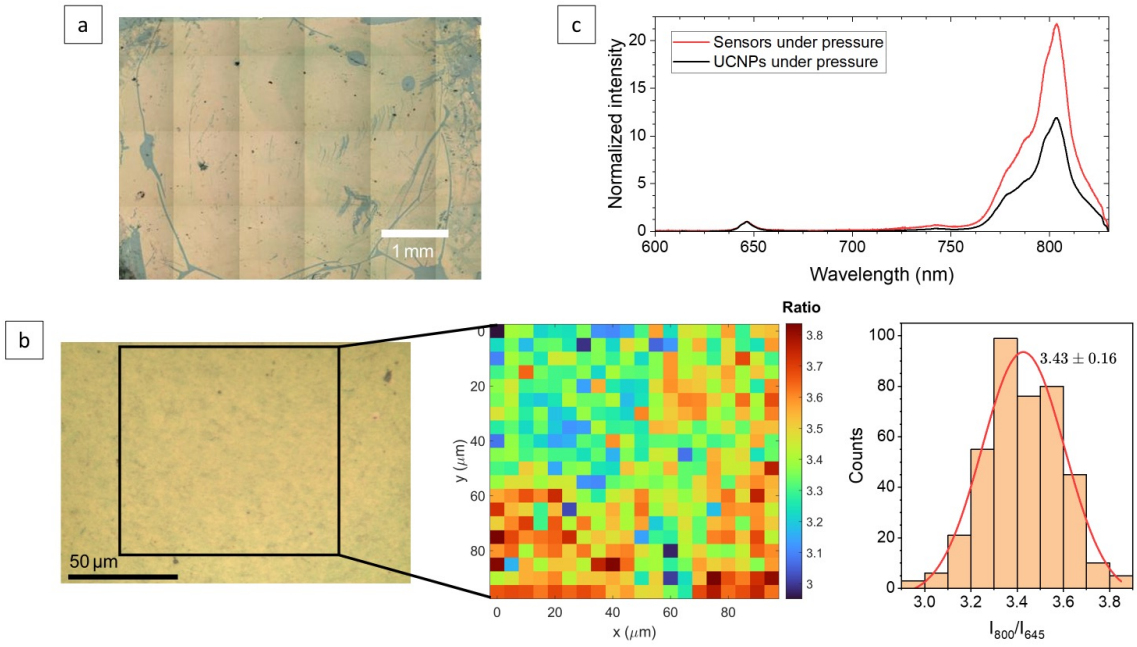

Figure 4. (a) Optical micrographs of the nanosensor array. (b) Left: Optical micrographs of the nanosensor array, under 50x magnification. Middle: PL intensity ratio map over 100 µm x 100 µm area obtained by confocal scanning under 980 nm excitation. Right: Histogram of PL intensity ratio over the area shown in the middle plot. (c) PL spectra of UCNP monolayer and the nanosensor array under 980 nm excitation measured under identical conditions. The spectra are normalized to the 645 nm peak intensity in order to highlight the selective enhancement of 800 nm emission line.

Finally, the nanosensors were characterized under applied force using two different methods. In one approach inspired by Kim et al.,[29] the nanosensors are compressed by a borosilicate glass stamp attached to a translation stage (Figure S4). Using a stamp with a well-defined area allows us to accurately calculate the force per nanosensor. The translation stage enables us to control the deformation directly. However, most motorized translation stages have a minimum translation resolution of 100 nm or larger and thus cannot produce the nanometer-scale deformations needed for our nanosensor characterization. To circumvent this issue, we added a 5 mm-thick PDMS load bearing layer under the nanosensors. In this configuration, most of the strain induced by the translation stage is absorbed by the load bearing layer and the nanosensors experience only small compression. A simple textbook analysis shows that the relative strain in each layer in this system will be inversely proportional to the elastic coefficient.[30] This allows us to determine the force exerted on the nanosensors. The PDMS load bearing layer and the nanosensor array are separated by a rigid glass slide in order to prevent any non-uniform deformation. Details of the setup and the analysis are given in the Supporting Information.

Figure 5(a) shows the PL intensity ratio map over an area containing a glass stamp. The circular region at the center is pressed down by the stamp, while the region outside remains undisturbed. The figure clearly shows that the nanosensors under the stamp exhibit higher PL

intensity ratio, consistent with the nanosensors being under compressive force. In contrast, the nanosensors outside the stamp do not show any change. This is direct evidence that our nanosensors respond to the applied force as designed. Figure 5(b) shows the individual PL intensities and the intensity ratio measured at various values of applied forces. Initially, the PL intensities and the intensity ratio remain constant until the stamp contacts the nanosensor array. Once the stamp starts pressing down the nanosensors, the 800 nm intensity increases while 645 nm intensity remains unchanged, increasing the intensity ratio. The 800 nm intensity and the intensity ratio eventually saturate when the PDMS layer reaches the elastic limit. The applied force on the nanosensor array is calculated by the measured strain of the PDMS load bearing layer and its Young's modulus. By dividing the total force applied by the number of nanosensors under the stamp, we determine that each nanosensor is responsive to forces in the range of 100's nN and saturates at around 2 μN, as shown in Figure 5(b). We could extract the force responsivity (defined as the ratio of signal change per applied force change) from the slope, which was 0.3 μN^{-1}. A recent work on UCNP-based force sensing reported a pressure responsivity of 0.4 GPa^{-1}.[18b] Since our nanosensor has a cross-sectional area of 1.77 x 10^4 nm^2 (150 nm diameter), our force responsivity corresponds to a pressure responsivity of 5.3 GPa^{-1}, an order of magnitude improvement. We note that the error bars in Figure 5(b) are larger than the variations observed in Figure 4. This arises from the difficulty of precisely controlling the stamp and the resulting uneven pressing of our sensors during the measurements. Thus, Figure 4 is the better representation of the real sensor-to-sensor variations.

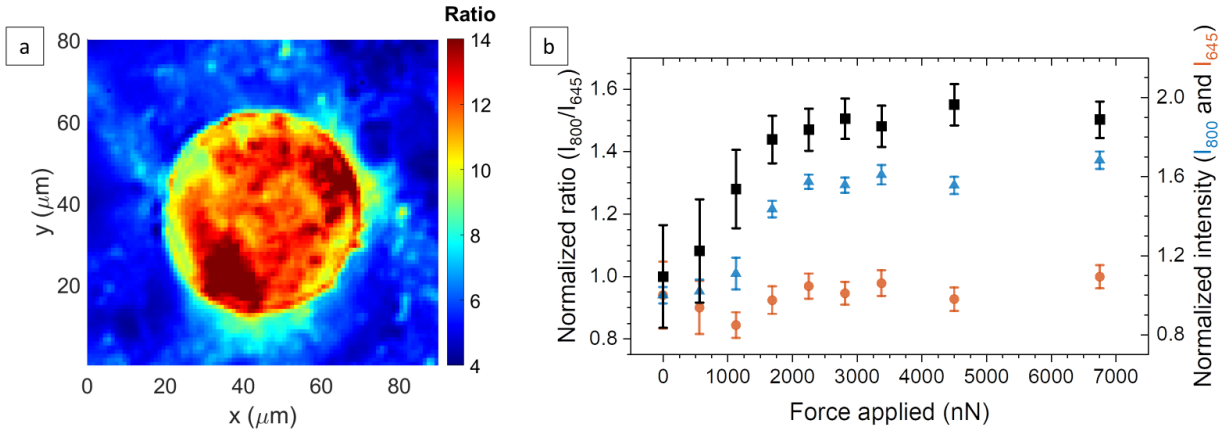

Figure 5. (a) PL intensity ratio map over an area containing a glass stamp. (b) PL intensity ratio and normalized intensities at 645 nm and 800 nm as a function of applied force.

To expand the applicability of our nanosensors, we fabricated another version incorporating a softer PDMS formulation. In the nanosensor presented in Figure 5, we used Sylgard 184, which has a bulk Young's modulus of 1 MPa. In the new version, we used a mixture of Sylgard 184 with Sylgard 527, which has a bulk Young's modulus of 100 KPa.[31] With a softer PDMS layer, the nanosensor should be responsive to smaller forces. Using the setup described

above, however, it was difficult to produce small enough forces even with the PDMS load bearing layer. We therefore used a gas pressure chamber instead (See Figure S5 and related texts). Simply placing the nanosensors in a pressurized chamber, however, will not properly compress them because the gas pressure will be applied not only on the top surface but also on the side as well. This will prevent the PDMS layer from expanding laterally as it gets compressed vertically. In order to apply force only along the vertical direction, we vacuum-sealed our nanosensor array with a plastic sheet. In this setup, the gas pressure is applied uniformly on the plastic cover, exerting vertical force on the nanosensors. Figure 6 shows the sensor response as a function of applied force. The PL intensity ratio increases gradually in the force range of 70 ~ 740 nN, roughly an order of magnitude smaller than that in Figure 5. This is the consequence of using a softer PDMS formulation in this nanosensor. It was not clear whether the nanosensor reached saturation at ~740 nN, which was the maximum force we could generate using the gas pressure chamber. This result illustrates that one can engineer the sensitivity by adjusting the elastic modulus of the flexible polymer layer in the nanosensor. We anticipate that further engineering the PDMS formulation will likely lower the minimum measurable forces down to ~1 nN. The force sensitivity obtained from the slope of Figure 6 was 2 μN^{-1}. This corresponds to a pressure responsivity of 35 GPa^{-1}, which is two orders of magnitude larger than that of the alkaline earth UCNP force sensor.[18b]

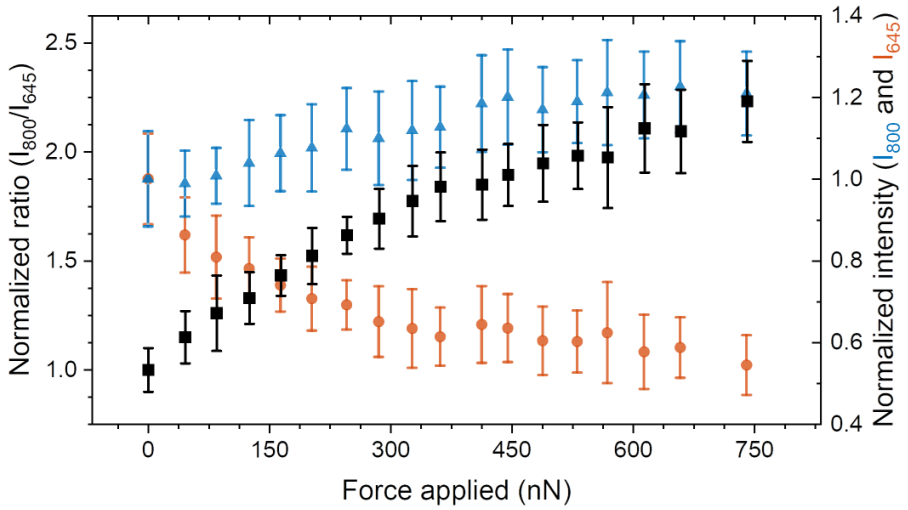

Figure 6. PL intensity ratio as a function of applied force using the nanosensor fabricated with a softer PDMS formulation. The experiments were carried out in a gas pressure chamber to allow us to produce forces on the order of 80 nN.

It is noted that the PL intensity ratio increase in Figure 6 is the result of both the decrease in 645 nm intensity and increase in 800 nm intensity. The different behaviors observed in Figures 5 and 6 are the consequence of the difference in excitation powers used in the two experiments. The window in our gas pressure chamber exhibits absorption in the near-infrared region. Thus, the laser power reaching the nanosensors was substantially lower in the pressure chamber than

in the direct pressing experiments. As shown in the detailed rate equations analysis in the Supplementary Information, there is a delicate interplay between Purcell enhancement, energy transfer and absorption enhancement. This results in a nontrivial dependence on the pump power. Our analyses show that, at high pump powers, the PL intensity ratio increases with increasing strain due mainly to increasing 800 nm intensity. At lower pump powers, however, 800 nm intensity increases only slightly while the 645 nm intensity decreases, consequently increasing the PL intensity ratio. These analyses correctly describe the experimental results in Figures 5 and 6. The full details of the analyses are presented in the Supporting Information. It is noted that the PL intensity ratio displays the expected increase with increasing external force in both cases, despite the different behaviors of individual intensities. This is another example of the benefits of ratiometric sensing.

Conclusions

We present a novel force sensor based on the plasmon modulated upconversion luminescence. By exploiting the short-range nature of plasmon interaction, the nanosensor is responsive to nanoscale deformations, which in turn allows for precise sensing of small forces. Since the near-infrared light interacts minimally with biological tissues, the use of near-infrared excitation makes the nanosensors well suited for biosensing applications. Furthermore, the new nanosensor employs a ratiometric sensing scheme in which one luminescence band serves as the signal while the other one acts as reference. The ratiometric sensing is much robust against environmental variations than the fluorescence intensity-based sensing scheme. The nanosensors are also very small, ~150 nm in diameter, and fabricated in a massive array. This enables sensing with high spatial resolution. This feature is particularly attractive for tactile sensing in robots where most tactile sensors lack high spatial resolution.

To experimentally demonstrate the novel nanosensor, we developed a new fabrication process that combines laser interference lithography, nanoparticle self-assembly, pattern transfer, and wet and dry etching. We obtained a highly uniform nanosensor array containing several hundred million sensors. The variations in the sensor dimensions were very small. The gold nanodisk sizes had variations less than 3% while the sensor heights showed variations of 6%. The excellent uniformity was further confirmed by the PL intensity measurements which exhibited 5% variations across the sample. We then built two force characterizations setups to demonstrate force sensing. The two versions of nanosensors incorporating two different formulations of PDMS can detect forces in the range of 70 nN to 2 μN, with force responsivities of 0.3 and 2 μN^{-1}, which are orders of magnitude larger than those reported for recent UCNP-based force sensors. Here, we report nanosensor arrays on glass substrates, but it is also possible to disperse the nanosensors in water using a process we demonstrated in our previous publication.[23] This would then allow direct injection into tissues for 3D *in vivo* measurements.

Acknowledgments

The work is supported in part by the National Science Foundation (CBET 2029559), National Institute of Health (R21 GM140347), Department of Education (GAANN P200A180012, P200A210111) and Colorado Office of Economic Development and International Trade (DO 2023-2330).

Competing interest

W. P. has a stake in Irradiation Sensing Corp. The remaining authors have no competing interests to declare.

References

[1] B. Zhou, B. Shi, D. Jin, X. Liu, *Nature Nanotechnology* **2015**, 10, 924.

[2] F. Auzel, *Chem Rev* **2004**, 104, 139.

[3] S. Wu, G. Han, D. J. Milliron, S. Aloni, V. Altoe, D. V. Talapin, B. E. Cohen, P. J. Schuck, *Proc Natl Acad Sci U S A* **2009**, 106, 10917.

[4] M. S. Arai, A. S. S. de Camargo, *Nanoscale Adv* **2021**, 3, 5135.

[5] a)M. K. Mahata, K. T. Lee, *Nanoscale Advances* **2019**, 1, 2372; b)C. Corbella Bagot, E. Rappeport, A. Das, T. Ba Tis, W. Park, *Advanced Optical Materials* **2022**, 10, 2200242.

[6] Q. Liu, Y. Sun, C. Li, J. Zhou, C. Li, T. Yang, X. Zhang, T. Yi, D. Wu, F. Li, *ACS Nano* **2011**, 5, 3146.

[7] a)R. Gao, C. Hao, L. Xu, C. Xu, H. Kuang, *Anal. Chem.* **2018**, 90, 5414; b)D. Giust, M. I. Lucio, A. H. El-Sagheer, T. Brown, L. E. Williams, O. L. Muskens, A. G. Kanaras, *ACS Nano* **2018**, 12, 6273.

[8] L. Mattsson, K. D. Wegner, N. Hildebrandt, T. Soukka, *RSC Advances* **2015**, 5, 13270.

[9] a)D. Lu, C. Mao, S. K. Cho, S. Ahn, W. Park, *Sci. Rep.* **2016**, 6, 18894; b)W. Park, D. Lu, S. Ahn, *Chem. Soc. Rev.* **2015**, 44, 2940; c)D. Lu, S. K. Cho, S. Ahn, L. Brun, C. J. Summers, W. Park, *ACS Nano* **2014**, 8, 7780.

[10] D. A. W. Thompson, *On Growth and Form*, Cambridge University Press, Cambridge, England **1942**.

[11] A. J. Engler, S. Sen, H. L. Sweeney, D. E. Discher, *Cell* **2006**, 126, 677.

[12] E. Farge, *Curr. Biol.* **2003**, 13, 1365.

[13] F. Bosveld, I. Bonnet, B. Guirao, S. Tlili, Z. Wang, A. Petitalot, R. Marchand, P. L. Bardet, P. Marcq, F. Graner, Y. Bellaiche, *Science* **2012**, 336, 724.

[14] R. Sunyer, V. Conte, J. Escribano, A. Elosegui-Artola, A. Labernadie, L. Valon, D. Navajas, J. M. Garcia-Aznar, J. J. Munoz, P. Roca-Cusachs, X. Trepat, *Science* **2016**, 353, 1157.

[15] Y. A. Miroshnikova, J. K. Mouw, J. M. Barnes, M. W. Pickup, J. N. Lakins, Y. Kim, K. Lobo, A. I. Persson, G. F. Reis, T. R. McKnight, E. C. Holland, J. J. Phillips, V. M. Weaver, *Nat. Cell Biol.* **2016**, 18, 1336.

[16] T. R. Dargaville, B. L. Farrugia, J. A. Broadbent, S. Pace, Z. Upton, N. H. Voelcker, *Biosensors and Bioelectronics* **2013**, 41, 30.

[17] a)S. Pyo, J. Lee, K. Bae, S. Sim, J. Kim, *Adv. Mater.* **2021**, 33, e2005902; b)W. Othman, Z. A. Lai, C. Abril, J. S. Barajas-Gamboa, R. Corcelles, M. Kroh, M. A. Qasaimeh, *Front Robot AI* **2021**, 8, 705662.
[18] a)A. Lay, D. S. Wang, M. D. Wisser, R. D. Mehlenbacher, Y. Lin, M. B. Goodman, W. L. Mao, J. A. Dionne, *Nano Lett.* **2017**, 17, 4172; b)C. A. McLellan, C. Siefe, J. R. Casar, C. S. Peng, S. Fischer, A. Lay, A. Parakh, F. Ke, X. W. Gu, W. Mao, S. Chu, M. B. Goodman, J. A. Dionne, *J Phys Chem Lett* **2022**, 13, 1547.
[19] N. Hildebrandt, M. Lim, N. Kim, D. Y. Choi, J. M. Nam, *Chem Commun (Camb)* **2023**, 59, 2352.
[20] E. M. Purcell, *Phys. Rev.* **1946**, 69, 681.
[21] P. Anger, P. Bharadwaj, L. Novotny, *Phys. Rev. Lett.* **2006**, 96, 113002.
[22] K. Bae, B. Xu, A. Das, C. Wolenski, E. Rappeport, W. Park, *RSC Advances* **2021**, 11, 18205.
[23] A. Das, C. Mao, S. Cho, K. Kim, W. Park, *Nat. Commun.* **2018**, 9, 4828.
[24] A. Das, C. Corbella Bagot, E. Rappeport, T. Ba Tis, W. Park, *J. Appl. Phys.* **2021**, 130, 023102.
[25] F. Reincke, W. K. Kegel, H. Zhang, M. Nolte, D. Wang, D. Vanmaekelbergh, H. Mohwald, *Phys. Chem. Chem. Phys.* **2006**, 8, 3828.
[26] J. Pu, Y. Yomogida, K. K. Liu, L. J. Li, Y. Iwasa, T. Takenobu, *Nano Lett.* **2012**, 12, 4013.
[27] S. K. Cho, L.-J. Su, C. Mao, C. D. Wolenski, T. W. Flaig, W. Park, *Materials Science and Engineering: C* **2019**, 97, 784.
[28] X. Ye, J. E. Collins, Y. Kang, J. Chen, D. T. N. Chen, A. G. Yodh, C. B. Murray, *Proc. Natl. Acad. Sci. U.S.A.* **2010**, 107, 22430.
[29] M.-S. Kim, J.-H. Choi, Y.-K. Park, J.-H. Kim, *Metrologia* **2006**, 43, 389.
[30] F. Beer, P;, E. R. Johnston Jr., J. T. Dewolf, D. Mazurek, F.;, *Mechanics of Materials*, McGraw-Hill, **2012**.
[31] R. N. Palchesko, L. Zhang, Y. Sun, A. W. Feinberg, *PLoS One* **2012**, 7, e51499.

Optical force sensor based on plasmon modulated upconversion luminescence

Conrad Corbella Bagot[1], Taleb Ba Tis[2], Bo Xu[3], Cobi Sabo[1], Eric Rappeport[1] and Wounjhang Park[1,3,4]
[1]Department of Electrical, Computer and Energy Engineering
[2]Materials Science and Engineering Program
[3]Department of Physics
[4]Biomedical Engineering Program
University of Colorado, Boulder, CO 80309-0425, U.S.A.

Supporting Information

1. Synthesis and characterizations of $NaYF_4$:Yb,Tm upconversion nanoparticles

Materials: $YCl_3 \cdot 6H_2O$, $YbCl_3 \cdot 6H_2O$, $TmCl_3$, oleic acid (technical grade, 90%) (OA), 1-octadecene (technical grade, 90%) (ODE), and ammonium fluoride (NH_4F) were bought from Sigma-Aldrich. Solid sodium hydroxide (NaOH) pellets were purchased from Fisher Scientific.

Synthesis: 24.7%, 0.3 % Yb^{3+}/Tm^{3+}-doped UCNPs were synthesized via the thermal coprecipitation method, with some modifications.[1] Briefly, 455 mg $YCl_3 \cdot 6H_2O$, 191.4 mg $YbCl_3 \cdot 6H_2O$, and 1.65 mg $TmCl_3$ were added to 36 mL ODE and 12 mL OA and heated under vacuum at 160℃ for 30 minutes. A 20 mL methanol solution containing 200 mg NaOH and NH_4F was separately prepared. The ODE/OA solution was cooled down to 50℃, opened to atmosphere, and the methanol solution was added dropwise. This mixed solution was stirred for 30 minutes at 50℃, then heated to 100℃ and put under vacuum for 20 minutes. The flask was then put under an argon atmosphere and heated to 300℃ at a rate of 10℃/min. The solution was left at 300℃ for 2 hours, cooled down naturally to less than 60℃, and transferred to two centrifuge tubes. Ethanol was added to the tubes to induce flocculation, and the UCNPs were collected by centrifugation (5400g, 10 minutes). The supernatant was removed, and the UCNPs were redispersed in hexane. Ethanol was added again, and the particles were centrifuged (5400g, 10 minutes). This redispersion process was repeated one more time.

Characterization: Transmission Electron Microscopy (TEM) images of the UCNPs were obtained using a Tecnai T12 Spirit 120kV Electron Microscope. Particle size was calculated via the ImageJ software package. Several hundred nanoparticles were used to assess the size statistics (Figure S1).

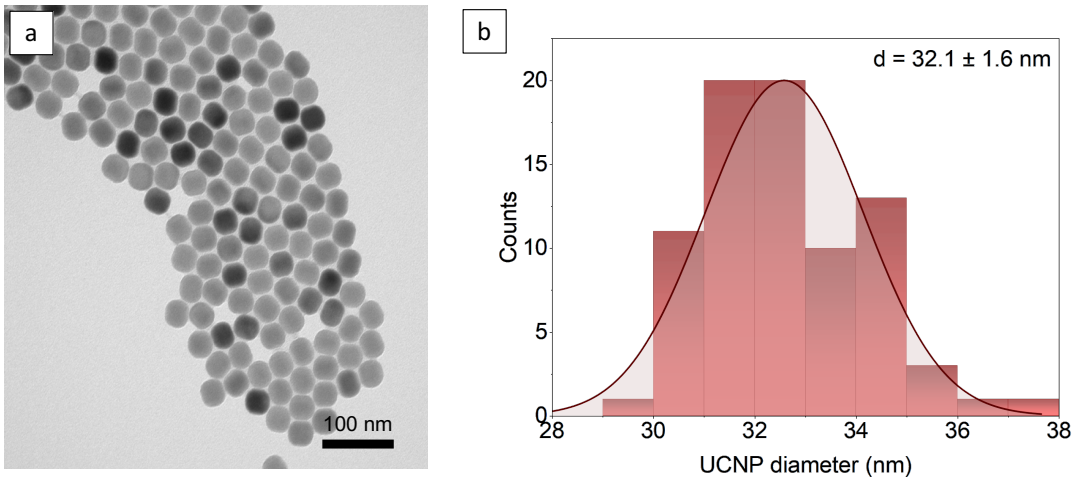

Figure S1. (a) Transmission electron micrograph (TEM) of $NaYF_4$:Yb,Tm UNCPs used in this work. (b) Histogram of size distribution showing a mean size of 32.6 nm and standard deviation of 1.6 nm.

2. Nanosensor fabrication process details

Self-assembly of upconverting nanoparticle monolayer

This method was adopted from Ren et. al.[2] with some modifications. First, a stock solution of $NaYF_4$:Yb^{3+}, Tm^{3+} nanocrystals was prepared in $CHCl_3$ and allowed to settle down overnight. In a 50 mL glass beaker, 30 µL (equivalent to 0.03 mg UCNPs) was drawn from the clear portion of the stock solution and added to 30 mL $CHCl_3$. The solution was then sonicated for 30 seconds to ensure uniform UCNPs dispersion. DI water was gradually added to the beaker until it slightly overflowed, and then 200 µL of ethanol was carefully delivered just below the chloroform/water interface over a period of 5 to 10 seconds using a burette. After that, the burette was gently lifted, and the solution was allowed to stabilize for 10 minutes. The water layer was gradually removed until the surface tension of the $CHCl_3$ ruptured the water layer, creating a water ring around the beaker's edges. If needed, additional water droplets may be added to expand the water ring for easier scooping of the monolayer. After the ring formation, the beaker was covered with a watch glass and left to stabilize for another 15 minutes. Finally, a 1.5x1.5 cm^2 coverslip was gently inserted at the edge of the water ring and lifted at an angle to collect the UCNP monolayer film from the water/air interface. The coverslips containing the UCNPs were cleaved into ~ 0.5x0.5 cm^2 substrates, which were then sonicated in $CHCl_3$ for 30 seconds to remove any large UCNPs aggregates or glass shards resulting from the cleaving step.

Spin-coating of PDMS thin film

Two commercially available silicone elastomer kits (SYLGARD 184 & SYLGARD 527, Dow Corning, USA) were used to fabricate the elastic spacer layers. As shown in a previous report,[3] the elasticity of PDMS can be tuned by blending these two formulations together. In this work, two different PDMS formulations were prepared to tune the responsivity of the sensors.

The first formulation contained only SYLGARD 184, with 10 parts of base per part of curing agent. The second formulation diluted 1 part of the first formulation with 10 parts of SYLGARD 527. The SYLGARD 527 was in turn prepared by combining an equal amount of part A and part B.

In both cases, the prepolymer base and curing agent were thoroughly mixed for 5 minutes in a clean weighing boat. The boat was then placed under vacuum until all air bubbles created during mixing were removed. Subsequently, a 2.5wt% stock solution of the PDMS mixture was prepared in hexane, vortexed for 5 minutes, and left to nutate overnight. Following this, few droplets of the PDMS stock solution were added onto the UCNP monolayer substrates, and spin-coated for 30 seconds at 5000 rpm under maximum acceleration. Finally, the PDMS-coated substrates were cured on a hotplate at 55 °C for 24 hours.

Fabrication of gold nanodisk array

A negative photoresist (NR9-1000PY, Futurrex) was first spun on a silicon wafer for 5 seconds at 500 rpm followed by 40 seconds at 8000 rpm. The wafer was then baked at 150 °C for 1 minute and cleaved into ~ 1x1 cm^2 small substrates for the lithography step. To create a hole array pattern on the resist layer, a home-built Llyod's mirror laser interference lithography setup with a 325 nm HeCd laser (Kimmon) was used to expose the substrates twice, with the substrates rotated 90 degrees the second time. The hole diameters can be tuned to 150 nm by adjusting the exposure conditions. After this, the substrates were baked at 100 °C for 1 minute before immersing them in the developer solution (RD-6, Futurrex) for 15 seconds. Following the lithography, a 30 nm thick gold layer was thermally evaporated onto the substrates to create the gold nanodisks. Finally, the remaining resist was lifted off by soaking the substrates in acetone and sonicating for 5-10 seconds. The size and uniformity of the fabricated hole and nanodisk arrays were characterized using a field-emission scanning electron microscope (FESEM, JEOL JSM-7401F) as shown in Figure S2.

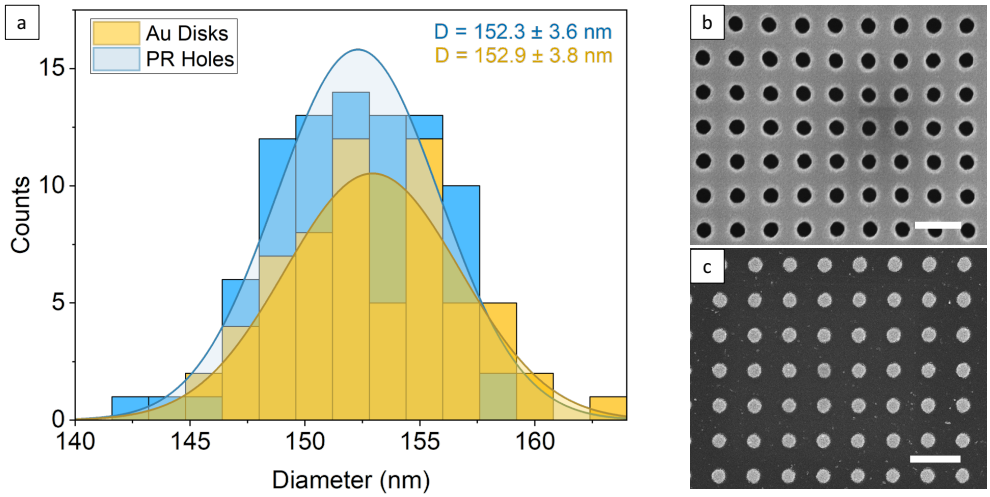

Figure S2. (a) Size distribution of PR holes and gold disks, calculated from the SEM images, presented in (b) and (c), respectively. Scale bars are 500 nm long.

Gold disk transfer

The nanopattern transfer method was adopted from Pu et. al.[4] with some modifications. First, a 4% solution of polymethylmethacrylate (PMMA) in anisole was spun on the gold nanodisks substrate, followed by baking at 185 °C for 5 minutes. After cooling down to room temperature, the edges of the PMMA film were carefully scratched off (~ 0.5 mm from each side) using a razor blade to expose the Si surfaces to the etchant in the next step. Subsequently, the PMMA-coated substrate was gently placed atop a 3% (w/w) NaOH solution. The temperature of the etching solution was maintained at ~ 100 °C using a water bath. Once the PMMA film carrying the gold nanodisk array separates from the carrier Si substrates, a microscope slide was used to scoop it and transfer it to a clean DI water bath. At this point, the PDMS-coated UCNP substrate was treated with O_2 plasma (30s, 50 W, and 8 sccm) to improve the PDMS adhesion with the gold nanodisks. The PMMA film was then transferred onto the treated-PDMS substrate and baked at 80°C for 5 minutes. Finally, the PMMA carrier film was removed from the PDMS-substrate by soaking in a hot acetone bath for another 5 minutes, followed by acetone and water rinse.

Dry and wet etching

The reactive ion etching chamber was first conditioned by performing O_2 ashing for 10 minutes using a flow rate of 200 sccm and RF power of 500 W. Secondly, the PDMS etching recipe was run for a duration of 30 seconds before the samples were introduced into the chamber. This step helps stabilize the plasma during the actual etching stage. The PDMS etching recipe consists of a 15:5 (sccm:sccm) mixture of Ar: CF_4, operating at an RF power of 200 W and a base pressure of 30 millitorr. When the preconditioning was completed, the sensor substrates were placed inside the RIE chamber, and the etching recipe was run again for a total of 120 seconds. Following the PDMS etching process, the background UCNPs were etched away by immersing the substrates in a magnetically stirred hydrochloric acid (HCl) solution (pH ~ 1.3) for 30 seconds, after which they were rinsed with water. The height of the nanosensors was characterized using atomic force microscopy (DriveAFM, Nanosurf) as shown in Figure S3.

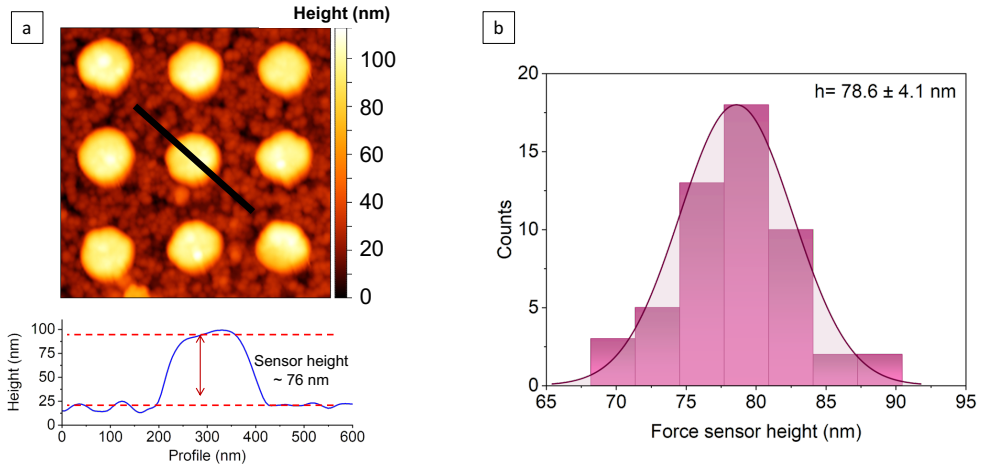

Figure S3. (a) Top: AFM map of the Tm sensors. Bottom: AFM profile of a Tm sensor (Au + PDMS + UCNPs). (b) Histogram of Tm sensors heights extracted from ~3x3μm^2 AFM map.

3. Nanosensor characterization

Two different methods were used to characterize the response of the sensors to external forces. In both scenarios, the photoluminescence (PL) spectroscopy was conducted using a confocal laser scanning microscope coupled with a spectrometer (Renishaw InVia). The samples were excited with a 980 nm wavelength laser (CrystaLaser DL980-500) and the emission from the sensors was collected for analysis. The samples were mounted on a 100 nm-resolution 3-dimensional translation stage so that we could monitor the PL signal changes from our sensors as the compression was varied. We developed two different ways to apply forces on the sensors.

Mechanical pressing setup

In the first method, the sample was compressed using a lens holder mounted on a translation stage with micrometer resolution (Figure S4a). As described in the figure (Figure S4 b and c), the sensors were compressed by a set of three 4 μm-tall, 50 μm-diameter circular stamps. Those stamps are used both to distribute the force applied by the flat glass mounted in the lens holder over a smaller number of sensors, increasing the pressure that the setup can produce, and to facilitate achieving uniform compression over the nanosensors, avoiding defects and dust particles on the sensor array.

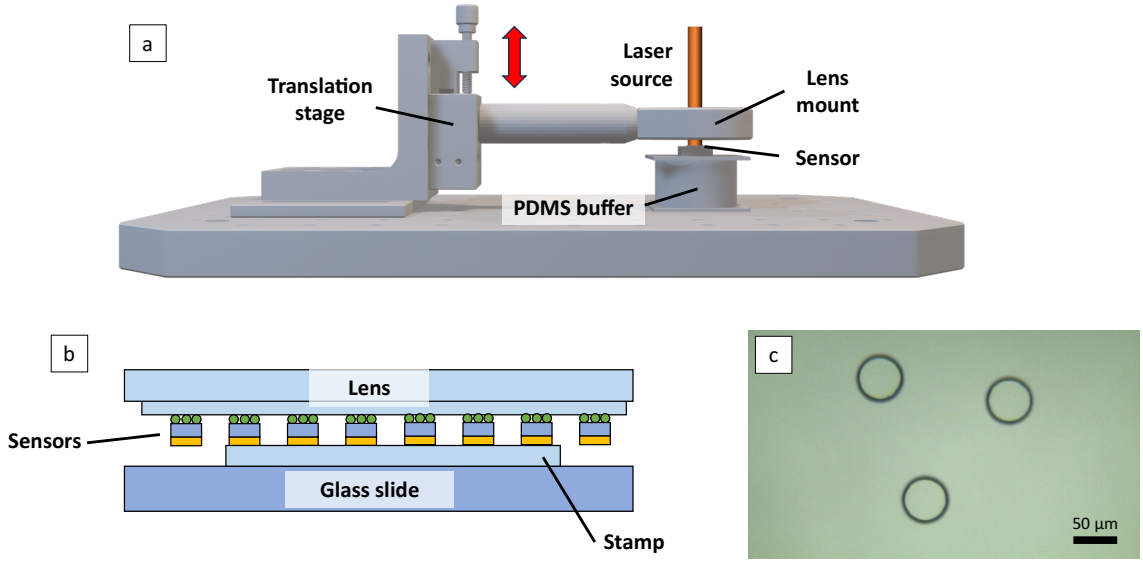

Figure S4. (a, b) Schematic of the custom force measurement setup in which the force sensors are compressed against a few 4 μm-tall glass stamps by a lens holder attached to a translation stage. The compression force is characterized by the deformation of the soft PDMS bearing layer and the top surface area of the glass stamps. In (b), a close up view of the sensor is presented. (c) Optical micrograph of three glass stamps fabricated on borosilicate substrate.

In order to fabricate the stamps, we spin-coated photoresist on a layer of $Ge_{28}Sb_{12}Se_{60}$ on glass. The PR was patterned by UV photolithography and then used as a mask to etch the $Ge_{28}Sb_{12}Se_{60}$ layer with KOH. Finally, BOE was used to etch the glass substrate. The PR and $Ge_{28}Sb_{12}Se_{60}$ masks were then removed, obtaining the stamps.

Under the sensors and stamps lies a thick piece of PDMS, which acts as a load bearing layer. The elastic modulus of the sensor, the glass substrates, and the stamp are orders of magnitude greater than that of the load bearing PDMS. Therefore, the equivalent elastic modulus of the compressed stack is approximately equal to the elastic modulus of the thick layer of PDMS. That is,

$$k_{eq} = \frac{1}{k_{glass}^{-1} + k_{PDMS}^{-1} + k_{SU8}^{-1} + k_{sensor}^{-1}} \sim k_{PDMS}$$

Given the travel distance of the actuator Δx and the elastic modulus of the 5 mm-thick PDMS layer [S3], we evaluate the force applied by the lens as $F \sim k_{PDMS}\Delta x$. Assuming a uniform distribution of that force over all the sensors under the stamps, we obtain that the force applied on each sensor is:

$$F_{sensor} = \frac{k_{PDMS}\Delta x}{3\pi R^2/p^2}$$

where R is the radius of the stamp and p is the spacing in between two adjacent sensors.

Gas pressure chamber setup

In the second method, the sample was mounted inside a customized *Instec* pressure chamber, connected to a nitrogen gas tank. The sample was sandwiched between two layers of plastic sheets that were sealed using a *FoodSaver* vacuum sealer. The plastic sheet was chosen to be rigid enough to maintain the pressure difference between inside and outside, so that the nanosensors are compressed along the vertical direction as the pressure in the chamber is increased. A schematic of the setup, the pressure chamber, and the nanosensors wrapped with the plastic sheets can be found on Figure S5(a), (b), and (c), respectively.

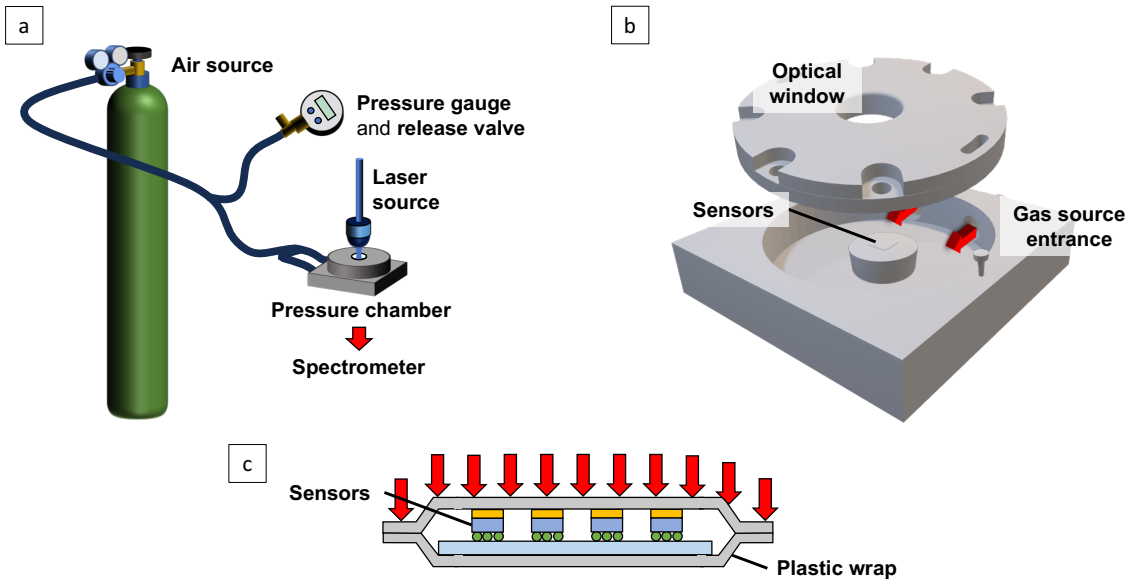

Figure S5. Schematics of the custom force measurement setup in which the force sensors are compressed under air pressure. (a) Depiction of the setup, including the air source, the pressure gauge used to measure the gas pressure, and the pressure chamber, where the sensor lies. (b) Drawing of the custom chamber used in the experiments. The red arrows indicate the entrance position for the gas. The samples were measured from the top, through the optical window. (c) Drawing of the sensors, wrapped around the plastic.

The applied pressure P was recorded using an Omega Digital Pressure Gauge DPG108-1.0KG and controlled using an AirGas Y11-N115H pressure gauge. Consequently, the force applied to each sensor is given by:

$$F_{sensor} = P \cdot period^2$$

where period is the period of the sensor array. When taking this measurement, we observe that, at the beginning, the 800 nm emission intensity increases rapidly with increasing pressure (see Figure S6). We ascribe this initial increase to the index change due to the plastic wrap making contact with the sensor surface. Initially, there is some air gap between the nanosensor surface and the plastic wrap, even though they are vacuum-sealed. Since the nanosensors are designed for the case where the nanosensor is mounted on a glass substrate and compressed by a stamp or plastic wrap, the plasmons resonance is detuned when there is an air gap between the nanosensor and plastic wrap. As the outside pressure is increased, the air inside gets pushed and compressed and eventually the plastic wrap makes contact with the nanosensor at which point the plasmon resonance is shifted to near 800 nm as designed. This leads to the rapid and large increase in 800 nm emission intensity at the beginning in Figure S6. As the pressure is further increased, the nanosensors begin to get compressed and the PL intensity changes due to compression. As shown in Figure S6, there is a clear difference in the slope of the PL intensity change between the two regions. We determined the onset of the nanosensor's response to the applied force by using the change in the slope between these two regions. This onset was further confirmed by the optical

micrographs taken during the measurements which showed the interference fringes in the measured regions begin to disappear near that point. This is also shown in Figure S6.

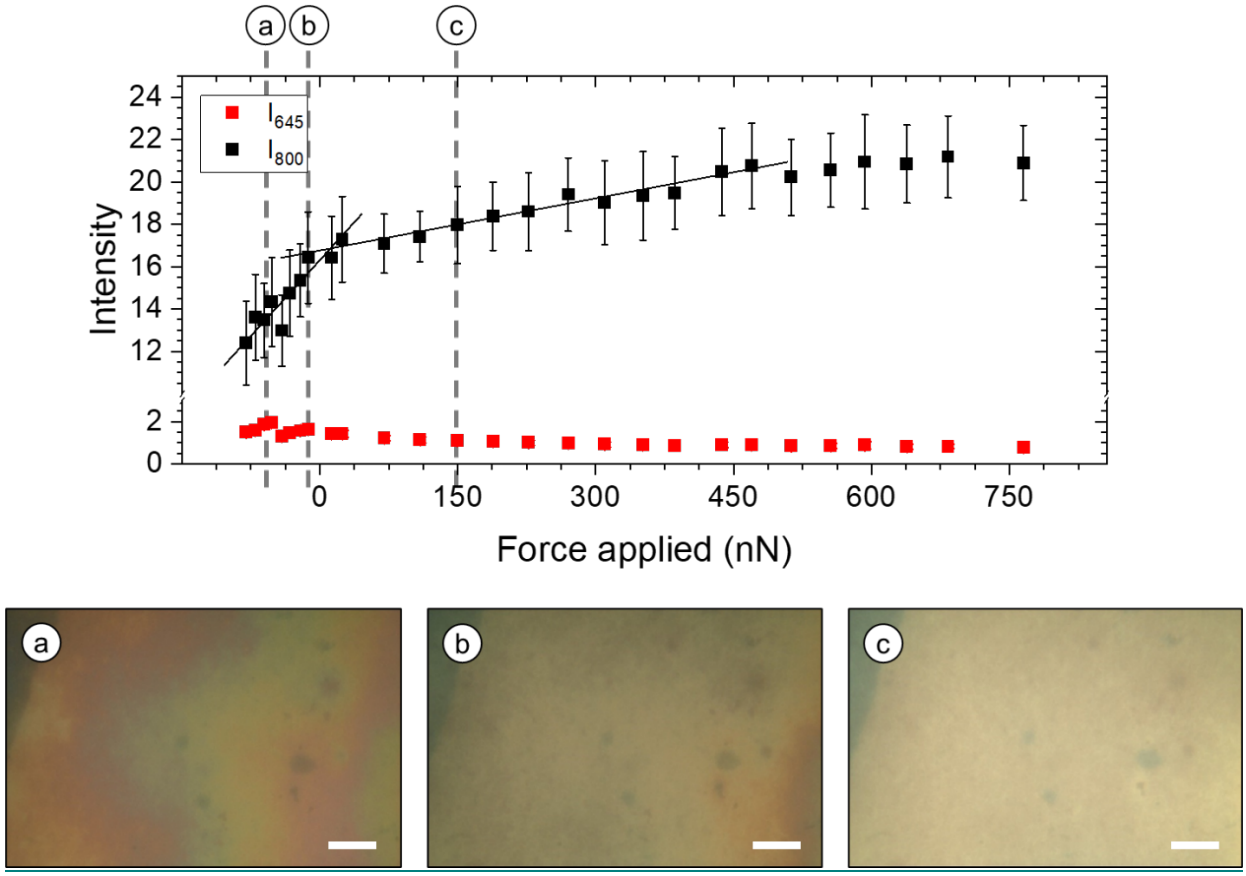

Figure S6. The change in the slope of the 800 nm emission is used as a reference to determine the point where the plastic completely wraps around the sensors. The micrographs on the bottom show the plastic clearly detached from the sensors in (a) and then attached in (c). In (b), one can still observe the plastic detached on the right side of the micrograph, indicating that the plastic got in contact with the sensors at a similar position than the slope changed.

Discussion on the possible deformations of the cover plastic under pressure

Covering the nanosensor array with a plastic sheet allows us to transfer the pressure exerted by the gas inside the pressure chamber onto the nanosensors. The plastic sheet is a particularly useful solution because it transforms a hydrodynamic pressure into a uniaxial one, exerted exclusively on the top of the gold disks. However, it is noted that this approach works only when the plastic sheets experience minimal to no deformations during the measurements. In this subsection, we will discuss the extent of that deformation, and the effects that it has on the metrics that we are monitoring.

In order to elucidate the effect of a possible deformation, we performed simulations using the commercial FEM software COMSOL. In these simulations, we used the elastic modulus of Nylon

between 200 MPa and 4 GPa.[5] For the PDMS layer within the nanosensor, the elastic modulus for such a thin film is expected to be larger than its bulks value of 100 kPa but it should still be at least an order of magnitude smaller than modulus of the plastic sheet.[6,7] Our simulations showed that, even with the smallest elastic modulus value (200 MPa) reported for the plastic sheet covering the sample, the gold nanodisks would not be embedded into the plastic by more than 5 nm (see Figure S7a). Also, the optical simulations similar to those presented in Figure 1 of the main text suggest that the gold nanodisks embedded into the plastic sheet by 5 nm would result in a very small decrease in the radiative lifetime of the 645 nm emission (Figure S7b). Our experiments did not show any measurable changes in the 645 nm emission lifetime. Therefore, we conclude that the possibility of plastic sheet deforms and gold nanodisks get embedded into the plastic is negligible.

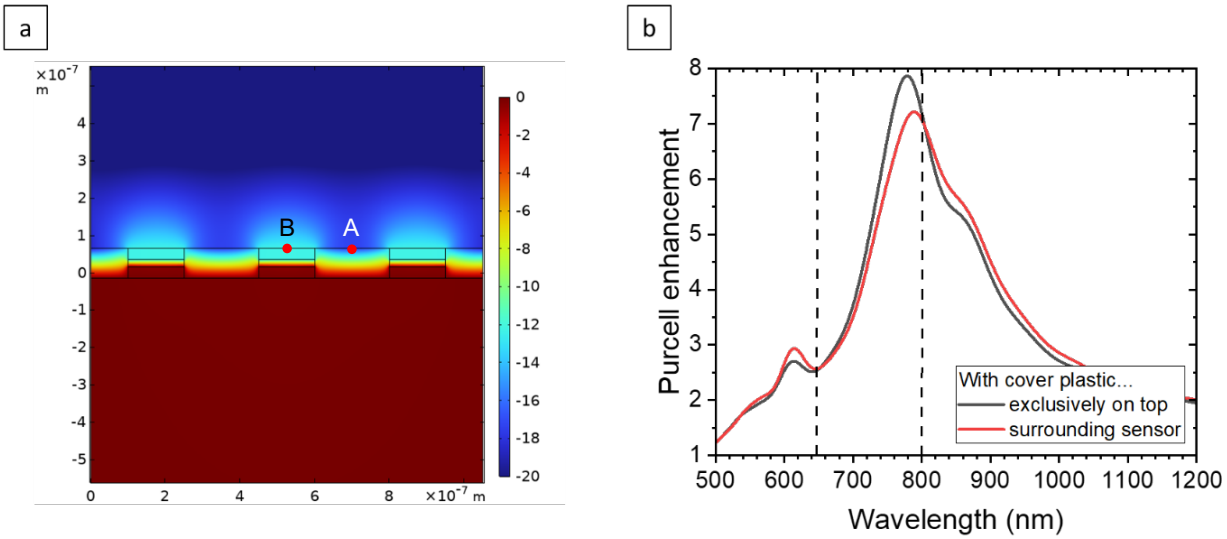

Figure S7. (a) Displacement field in the y-direction (in nm) predicted by a COMSOL simulation. The calculation assumes an elastic modulus of 200 MPa for the covering plastic, an elastic modulus of 10 MPa for the 20 nm PDMS spacer layer. The number reported above (4.7 nm) is computed as the difference in displacement between the central point between two adjacent gold disks (A) and the central point of that same gold disk (B). (b) FDTD simulation of the Purcell enhancement with the cover plastic exclusively on top, compared to the results predicted when the plastic cover also surrounds the top 5 nm of the gold nanodisks. The resonance is shifted to longer wavelengths, and the 645 nm enhancement is increased, but the difference between the two curves is small.

4. Simulations and rate equations analyses

A series of numerical simulations were performed for both the design of the nanosensor and the interpretation of the experimental data. In this section, we describe those three numerical simulations and discuss their results and consequences.

First, in order to quantify the Purcell enhancement effect on the lifetimes of the various UCNP emission lines, FDTD simulations were performed using the commercial software Lumerical

(Ansys). In these simulations, a dipole source (representing the emission of the UCNPs) was placed at different radial positions within the UCNP layer of the sensor. The power emitted by those dipoles was then integrated over a surface that completely enclosed the nanosensor. This value was then compared to the power emitted by a dipole in free space. The ratio between the two powers gives us the Purcell enhancement factor. These results are reported in Figure 1 of the main paper.

Second, we assess the effect of the gold nanodisk on the absorption of the UCNPs. Even though we designed the sensors to have a plasmon resonance at ~770 nm, the resonance is broad enough that it also affects the absorption of the 980 nm pump laser, similarly to what we reported in the past.[8] At low pump powers, the two emission bands discussed in this paper, 645 and 800 nm, exhibit different dependence on the pump intensity. This, in turn, influences the ratio between those two intensities, which is used to measure the applied force. In order to quantify this effect, we carried out FDTD simulations. In these simulations, we measured the change in the pump intensity in the UCNP layer as the PDMS thickness is reduced. To do that, we injected a plane wave centered at 980 nm, and monitored the electric field in the UCNP layer as shown in the schematic Figure S8(a). The results are presented in Figure S8b, which shows the increase in effective 980 nm intensity as a function of PDMS thickness.

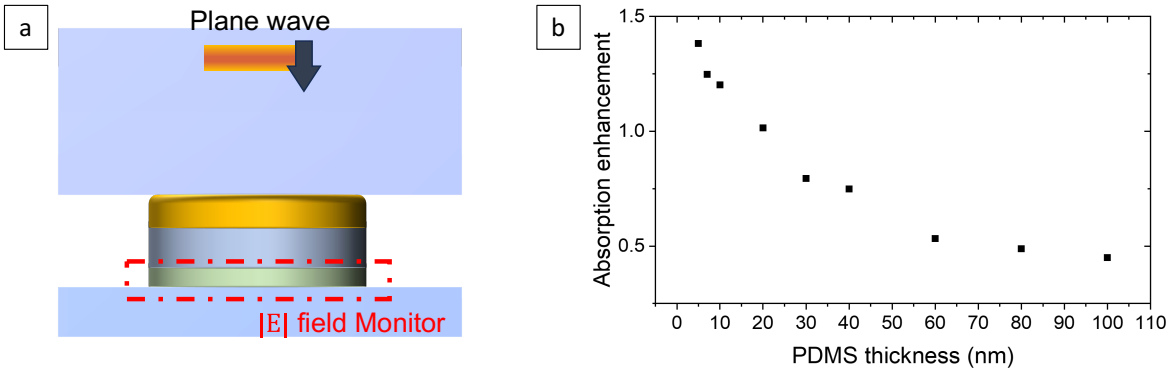

Figure S8. (a) Schematic of the FDTD simulation to compute the absorption enhancement as a function of the PDMS thickness. (b) Absorption enhancement as a function of PDMS thickness.

It should be noted that, due to the different power dependence of the 800 nm and 645 nm lines, absorption enhancement tends to decrease the I_{800}/I_{645} ratio as we compress the PDMS. This effect is opposite to the behavior desired for sensing. Fortunately, absorption enhancement is small and decreases further as the pump power is increased. Thus, the values reported in Figure S8(b) become relevant only at low pump intensities.

Finally, the enhanced radiative lifetimes and enhanced absorption cross-sections were fed into the rate equations governing the upconversion process:

$$\frac{dn_j^{Tm}}{dt} = c_{1,j} n_1^{Yb} n_{j-l}^{Tm} - c_{1,j+m}\, n_1^{Yb} n_j^{Tm} - \left(w_j^{rad} + w_j^{nr}\right) n_j^{Tm} + \sum_{k>j} \left(\beta_{kj} w_k^{rad} + w_{kj}^{nr}\right) n_k^{Tm} \pm \sum_{a,b} k_{ab}\, n_a n_b$$

$$\frac{dn_1^{Yb}}{dt} = \sigma^{Yb} I n_0^{Yb} - w_{Yb}^{rad} n_1^{Yb} - \sum_{j,l} c_{1,j} n_1^{Yb} n_{j-l}^{Yb}$$

where n_i^X is the population of the level i of the ion X, $c_{1,j}$ is the energy transfer rate between the top level of Yb^{3+} and the j-th level of Tm^{3+} ions,[9] w_j^{rad} and w_j^{nr} are the radiative and non-radiative decay rates of Tm^{3+},[10, 11] β_{kj} is the branching ratio from the level k to the level j of Tm^{3+},[10] k_{ab} are the cross-relaxation rates,[9] σ^{Yb} is the absorption cross-section of Yb^{3+},[12] I is the input intensity, and $l, m > 0$.

To include the Purcell effect, the Purcell enhancement factor γ_{ik} for a radiative transition between levels i and k (obtained by the Lumerical simulations) was multiplied to the relevant radiative decay rates. Specifically, the total radiative decay rate of level i is written as,

$$w_i^{rad} = w_i^{rad,0} \left(\sum_{j \neq k} \beta_{ij} + \beta_{ik} \gamma_{ik} \right)$$

where $w_i^{rad,0}$ is the free-space decay rate. For the absorption enhancement, we rewrite $\sigma^{Yb} = \Gamma_\sigma \sigma^{Yb,0}$, where Γ_σ is the absorption enhancement factor obtained from the FDTD simulations. With that, we obtain the results presented in Figure S9. In short, the rate equations suggest that even when considering the blended effect of absorption enhancement, the Purcell effect, and the excitation dynamics within Tm^{3+} ions, the nanosensors should continue to show an increase in the PL intensity ratio, I_{800}/I_{645}, as the distance between the gold nanodisk and the UCNPs is reduced. The detailed analyses, however, does reveal nontrivial dependence on the pump intensity. At high pump intensities, the effect of absorption enhancement is minimal, providing a behavior largely the same as what is predicted by the Purcell effect alone. At low pump intensities, however, the complex interplay between absorption enhancement, Purcell enhancement and energy transfer creates a region where the 800 nm intensity increases only slightly and 645 nm intensity decreases with decreasing PDMS thickness. These results agree with our experimental observations presented in Figures 5 and 6 in the main article.

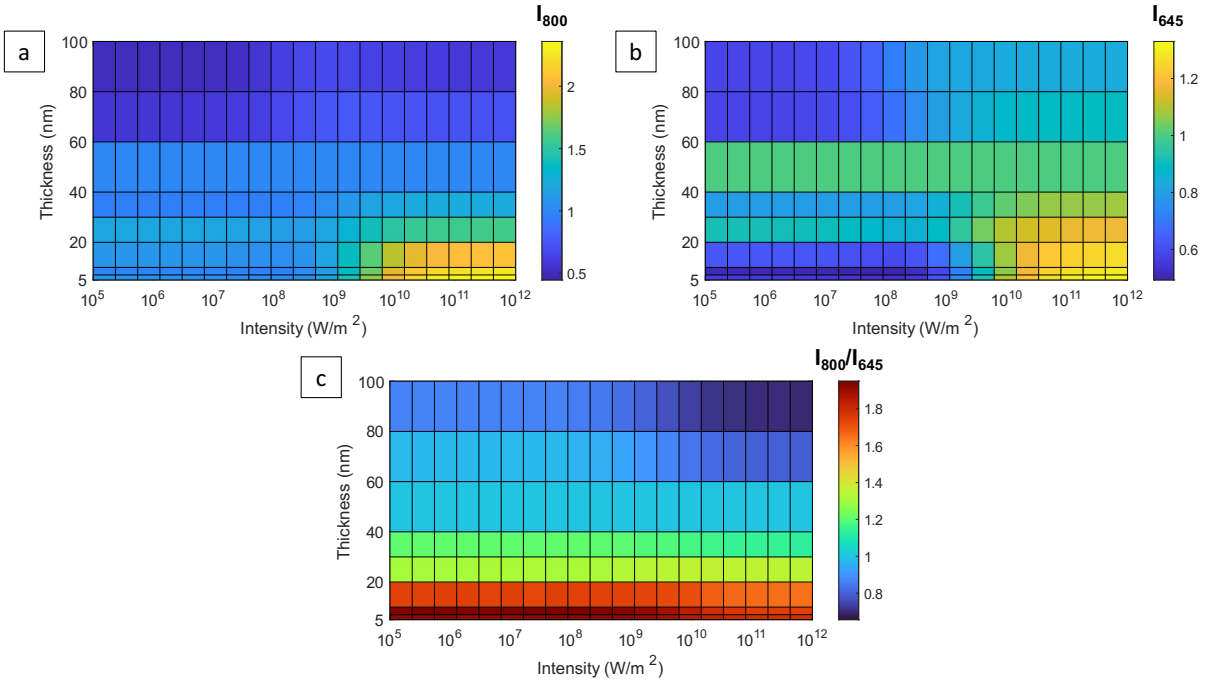

Figure S9. Rate equations analysis: (a) 800 nm intensity, (b) 645 nm intensity, and (c) intensity ratio for various PDMS thicknesses and pump intensities. All values are normalized to the intensity (or the ratio between the two lines) at the PDMS thickness of 100 nm.

As a final remark, we note that, while the simulations predict the behaviors observed in experiments, providing a strong proof that our nanosensor functions as designed, we do not have perfect match between the PL intensity ratios obtained by the simulations and the experiments. The highest enhancement factors for the PL intensity ratio observed in Figures 5 and 6 are approximately 1.6 and 2.0, respectively. These values are slightly higher than those predicted by the simulations which range between 1.4 ~ 1.8, depending on the pump power and PDMS thicknesses. There are several uncertainties related to the discrepancies. First, while we do know the initial thickness of the unstrained PDMS layer, we have no way of knowing the actual thickness of PDMS under applied force. Second, the window of the gas pressure chamber affects both transition and focusing, strongly affecting the collected luminescence signal. This is evident from the significantly lower luminescence intensity recorded from the pressure chamber experiments compared to the direct pressing experiments. But we have no means to directly measure the losses. Finally, the plastic wrap used in the pressure chamber experiments most likely would deform under pressure, affecting the plasmon resonance and consequently the local field profile and scattering patterns. This once again is not something that can be precisely measured and taken into account in the simulations.

While all of these uncertainties contribute to the small numeric discrepancies between simulations and experiments, we emphasize the simulations do predict precisely the behaviors observed in experiments, providing a strong support for the nanosensors potential for applications in biology, medicine and robotics.

References

1. Corbella Bagot, C.; Rappeport, E.; Das, A.; Ba Tis, T.; Park, W., True FRET-Based Sensing of pH via Separation of FRET and Photon Reabsorption. *Advanced Optical Materials* **2022,** *10* (15), 2200242.
2. Ren, Y.; Chen, M.; Hu, L.; Fang, X.; Wu, L., Oil/water interfacial self-assembly for the organization of hydrophobic NaYF4:Yb, Er nanoplatelets into closely-packed fluorescent nanofilms. *J. Mater. Chem.* **2012,** *22* (3), 944-950.
3. Palchesko, R. N.; Zhang, L.; Sun, Y.; Feinberg, A. W., Development of polydimethylsiloxane substrates with tunable elastic modulus to study cell mechanobiology in muscle and nerve. *PLoS One* **2012,** *7* (12), e51499.
4. Pu, J.; Yomogida, Y.; Liu, K. K.; Li, L. J.; Iwasa, Y.; Takenobu, T., Highly flexible MoS2 thin-film transistors with ion gel dielectrics. *Nano Lett.* **2012,** *12* (8), 4013-7.
5. Overview of materials for Nylon 66/6. https://www.matweb.com/search/datasheet_print.aspx?matguid=26386631ec1b49eeba62c80a49730dc4.
6. Xu, W.; Chahine, N.; Sulchek, T., Extreme hardening of PDMS thin films due to high compressive strain and confined thickness. *Langmuir* **2011,** *27* (13), 8470-7.
7. Thangawng, A. L.; Ruoff, R. S.; Swartz, M. A.; Glucksberg, M. R., An ultra-thin PDMS membrane as a bio/micro-nano interface: fabrication and characterization. *Biomed. Microdevices* **2007,** *9* (4), 587-95.
8. Das, A.; Mao, C.; Cho, S.; Kim, K.; Park, W., Over 1000-fold enhancement of upconversion luminescence using water-dispersible metal-insulator-metal nanostructures. *Nat. Commun.* **2018,** *9*, 4828.
9. Liu, Y.; Lu, Y.; Yang, X.; Zheng, X.; Wen, S.; Wang, F.; Vidal, X.; Zhao, J.; Liu, D.; Zhou, Z.; Ma, C.; Zhou, J.; Piper, J. A.; Xi, P.; Jin, D., Amplified stimulated emission in upconversion nanoparticles for super-resolution nanoscopy. *Nature* **2017,** *543* (7644), 229-233.
10. Villanueva-Delgado, P.; Biner, D.; Krämer, K. W., Judd–Ofelt analysis of β-NaGdF4: Yb3+, Tm3+ and β-NaGdF4:Er3+ single crystals. *J. Lumin.* **2017,** *189*, 84-90.
11. van Dijk, J. M. F., On the nonradiative and radiative decay rates and a modified exponential energy gap law for 4f–4f transitions in rare-earth ions. *J. Chem. Phys.* **1983,** *78* (9), 5317.
12. Strohhöfer, C. Optical properties of ion beam modified waveguide materials doped with erbium and silver. University Utrecht, 2001.